

**AN EFFICIENT METHOD FOR THE PERFORMANCE ANALYSIS OF
BOUNDED-WAVE NUCLEAR EMP SIMULATORS¹**

August 1992

J.J.A. Klaasen
Electromagnetic Effects Group
Netherlands Organization for Applied Scientific Research
TNO Physics and Electronics Laboratory
P.O.Box 96864
2509 JG The Hague
The Netherlands

ABSTRACT

The electromagnetic-performance analysis of bounded-wave Nuclear EMP (NEMP) simulators was carried out in the past by employing the (time-domain) Method of Moments (MoM) or conformal mapping. With the former, transient results can be obtained within the simulator's working volume. With conformal mapping the results are limited: the simulator's characteristic impedance and the static field distribution can be computed.

A problem associated with the MoM is that it yields a huge impedance matrix which for real-world simulators becomes prohibitively large. Either one can only employ the MoM for small simulators, or the number of wires that constitute the transmission-line structure has to be limited to an unrealistically low number.

In this paper, a new method will be enunciated that is extremely efficient, and enables one to analyze even the largest simulators. The method uses a priori knowledge as much as possible. It obtains the current in the wave-launcher's wires from an equivalent current filament of a conical-plate wave launcher that supports a TEM-mode. The transient electromagnetic fields within the simulator's working volume are then readily computed by using efficient and analytical time-domain expressions for the fields generated by the wires.

Expressions for the early-time fields and the impedance of a conical wire-mesh wave launcher are derived.

¹ This work was supported by the Royal Netherlands Navy, DMKM/PFS under contract 726.90.2006.

RECEIVED
20 NOV 1992
PL/SUL
KAFB, NM
47117-6008

TABLE OF CONTENTS

Section		Page
	ABSTRACT	1
1	INTRODUCTION	3
2	METHOD OF SOLUTION	4
	2.1 Waveform of the Current in the Wires of the Simulator	4
	2.2 Amplitude of the Current in the Wires of the Simulator	4
	2.3 Effects not Taken into Account by Our Model	7
3	VALIDATION OF THE METHOD OF SOLUTION	9
4	THE EARLY-TIME ELECTRIC FIELD EMITTED BY THE WAVE LAUNCHER	10
5	COMPARISON OF SOME RESULTS WITH MEASUREMENTS	13
6	A CASE STUDY: EMPSIS	15
	6.1 Calculation of the Characteristic Impedance of EMPSIS	15
	6.2 The Electromagnetic-Performance Analysis of EMPSIS	16
7	CONCLUSIONS	24
	REFERENCES	25
A	THE TRANSIENT ELECTROMAGNETIC FIELDS EMITTED BY A CURRENT-CARRYING STRAIGHT WIRE	A.1
	A.1 Formulation of the Problem	A.1
	A.2 Solution of the Problem	A.2

1 INTRODUCTION

The method described in this paper has been developed for the electromagnetic-performance analysis of a bounded-wave NEMP simulator for ships called EMPSIS (see Klaasen *et al.* [1]). The EMPSIS simulator and its performance are not the main subjects of this paper, but are merely used to illustrate the method outlined.

The electromagnetic-performance analysis of NEMP simulators was carried out in the past by employing the (time-domain) Method of Moments (MoM) or conformal mapping. With the former, transient results can be obtained within the simulator's working volume. With conformal mapping the results are limited: the simulator's characteristic impedance and the static field distribution can be computed (see Baum [2] and Giri *et al.* [3]).

Transient results can be obtained with the MoM (see Harrington [4], or Mittra *et al.* [5]) applied to thin wires in the time domain. Since the well-known NEC code (Burke and Poggio [6]) uses the MoM in the frequency domain, it is not particularly suited for transient analysis. De Haan *et al.* [7] used the NEC code for the performance analysis of the Lukksund experiment, but with limited results.

Bardet *et al.* [8] and Dafif *et al.* [9] applied the time-domain MoM to a Parallel-Plate Simulator (PPS) with dimensions $96 \times 20 \times 12$ m ($l \times w \times h$). Because of the available computer resources, they had to limit their analysis to a simulator consisting of 6 to 18 wires resulting in roughly 1500 wire segments, each with a length of 0.6 m. As a result of the new NEMP waveform definitions (see [10]) that took effect in November 1990, we now need a 0.3 m segment length, which increases the memory requirements even further by a factor of four. Therefore, the analysis of Bardet's simulator has to be limited to an unrealistic number of wires for the new waveform specification.

To compute the transient electromagnetic fields within the working volume of a simulator such as EMPSIS, with dimensions of $300 \times 168 \times 70$ m ($l \times w \times h$), we need something in the order of 1000 wire segments *per wire*. Obviously, the storage requirements and the computational costs² for such a large simulator become prohibitively large.

Therefore, from the above discussion we conclude that the MoM cannot be used for large real-world simulators. Hence, we have to employ another method than the MoM for a useful and practical performance analysis.

² To analyze a NEMP simulator made of four wires would take four hours CPU time on a CONVEX 230 mini super computer.

2 METHOD OF SOLUTION

The method of solution we have employed is based on the fact that if the transient current in each wire of the simulator is known, the electromagnetic fields generated by the simulator are known. This approach was also taken by King *et al.* [11] and [12], but for a rhombic wire simulator (a simulator for research purposes with the plates replaced by only two outer wires).

Since it is too much work (in a computational sense) to actually compute the current in each wire, we have taken a pragmatic approach that uses a priori knowledge as much as possible.

2.1 Waveform of the Current in the Wires of the Simulator

From experience, we know that the current in each wire of the wave launcher has a waveform similar to the current generated by the pulser (the AEP-4 edition 3 or edition 4 waveforms). Since the wires are uncoated, the current propagates towards the terminator at the speed of light. Furthermore, the current propagating along each wire does not change much in waveform and amplitude, so that we can simply assume its waveform and amplitude constant as it propagates.

These observations allow the use of efficient analytical time-domain expressions for the emitted electromagnetic fields of a current-carrying wire, which greatly simplify the analysis and reduce the computational costs.

2.2 Amplitude of the Current in the Wires of the Simulator

Although the waveform of the current in each wire is now known, we still have to determine its amplitude. We solve this by studying the TEM-mode current distribution of a conical-plate wave launcher that is excited at its apex. The amplitude of the current in each wire of the wire-mesh wave launcher is chosen in such a way that it closely corresponds with a current filament of the plate. In this way, the mutual interaction between the wires is taken into account.

In the next section, we will derive a relation between the current in the wires of the wire-mesh wave launcher and the current surface density of the conical-plate wave launcher.

2.2.1 Formulation of the Problem

First, each wire of the wire-mesh wave launcher runs parallel in the direction of propagation of the dominant radially directed current on the conical-plate wave launcher. The plate is infinitely thin, and is assumed to be excited at its apex in such a way, that the current surface density has a radially directed component only. In practice, such an excitation cannot be accomplished. However, this simplification is allowed as for the moment we are only interested in the surface current distribution that is associated with the TEM-mode generated by the plate, i.e., the radially directed component of the surface current.

The radially directed surface current has an azimuthal distribution, and its wavefront propagates with speed c_0 (the speed of light) along the plate. At this point, the azimuthal current distribution

is unknown, but will be discussed later.

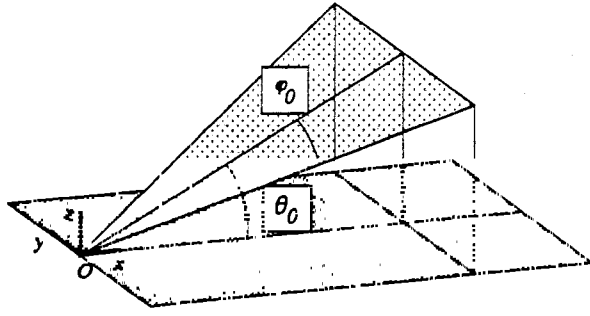


Figure 1 Conical-plate wave launcher.

The conical-plate wave launcher makes an elevation angle θ_0 with the x, y plane, and has an apex half-angle of φ_0 . The normal unit vector of the wave launcher pointing inwards the simulator volume is therefore given by

$$\underline{n} = \sin\theta_0 \underline{i}_x - \cos\theta_0 \underline{i}_z, \quad (1)$$

where $\underline{i}_x, \underline{i}_y$ and \underline{i}_z are the unit vectors in a orthogonal right-handed Cartesian reference frame. The apex of the wave launcher is located at \underline{s}_0 .

For the sake of convenience, the wave launcher is assumed to be of infinite extent in the radial direction.

The vector potential due to an arbitrary current source that occupies the volume V is given by

$$\underline{A}(\underline{r}, t) = \frac{\mu_0}{4\pi} \int_V \frac{\underline{J}(\underline{r}', t')}{R} dV(\underline{r}'), \quad \underline{r} \in \mathbb{R}^3 \quad (2)$$

where \underline{J} denotes the current volume density, and $R = |\underline{R}| = |\underline{r} - \underline{r}'|$. Furthermore, t' denotes the retarded time given by $t' = t - R/c_0$.

2.2.2 Solution of the Problem

The Vector Potential of a Conical-Plate Wave Launcher:

The current volume density reduces to a current surface density for the conical plate. Then the vector potential of Eq.(2) yields for a perfectly conducting, and infinitely thin conical plate

$$\underline{A}_{plate}(\underline{r}, t) = \frac{\mu_0}{4\pi} \int_S \frac{\underline{J}_s(\underline{r}', t')}{R} dA(\underline{r}'), \quad \underline{r} \in \mathbb{R}^3/S \quad (3)$$

where \underline{J}_s denotes the current surface density, and S the plate's surface. Using $\underline{r}' = \underline{s}_0 + \rho \underline{i}_\rho$, the current surface density is written as

$$\underline{J}_s(\underline{r}, t) = J_s(\underline{r}, t) \underline{i}_\rho = F(\varphi, \varphi_0) \frac{I(t - \rho/c_0)}{\rho} \underline{i}_\rho, \quad \underline{r} \in S \quad (4)$$

$F(\varphi, \varphi_0)$ is a function that governs the azimuthal distribution of the current surface density, and $I(t - \rho/c_0)$ accounts for the propagation in the radial direction. Furthermore, \underline{i}_ρ is the unit vector in the radial direction (the propagation direction). The latter is given by

$$\underline{i}_p = \cos\varphi \cos\theta_0 \underline{i}_x + \sin\varphi \underline{i}_y + \cos\varphi \sin\theta_0 \underline{i}_z. \quad (5)$$

The total current injected at the apex is given by

$$\begin{aligned} I_0(t) &= \lim_{\rho \rightarrow 0} \int_{-\varphi_0}^{\varphi_0} \rho \underline{J}_s(\underline{r}', t) \cdot \underline{i}_p \, d\varphi = \lim_{\rho \rightarrow 0} \int_{-\varphi_0}^{\varphi_0} F(\varphi, \varphi_0) I(t - \frac{\rho}{c_0}) \, d\varphi \\ &= \int_{-\varphi_0}^{\varphi_0} F(\varphi, \varphi_0) \, d\varphi \, I(t). \end{aligned} \quad (6)$$

We can associate $I(t)$ with the total current injected at the apex when the following normalization is used

$$\int_{-\varphi_0}^{\varphi_0} F(\varphi, \varphi_0) \, d\varphi = 1. \quad (7)$$

Such a normalization can always be carried out. An approximation of the TEM current distribution in a plate was presented by Giri [13]. For a conical plate, we deduce

$$F(\varphi, \varphi_0) = \frac{1}{\pi \sqrt{\varphi_0^2 - \varphi^2}}. \quad (8)$$

Note that the current distribution has the proper square-root singularity near the plate's edge, and complies with the normalization condition of Eq.(7).

The vector potential of the plate is finally rewritten as

$$\underline{A}_{\text{plate}}(\underline{r}, t) = \frac{\mu_0}{4\pi} \int_0^\infty \int_{-\varphi_0}^{\varphi_0} \underline{i}_p F(\varphi, \varphi_0) \frac{I_0(t - (\rho + R)/c_0)}{R} \, d\varphi \, d\rho. \quad (9)$$

Note that along the plate we have $\underline{r}' = \underline{s}_0 + \rho \underline{i}_p$, so that $R = |\underline{r} - (\underline{s}_0 + \rho \underline{i}_p)|$.

The Vector Potential of a Conical Wire-Mesh Wave Launcher:

For a straight wire, which for the sake of convenience is assumed to be of infinite length, that runs from the wave-launcher's apex with an azimuthal angle φ_i , and an elevational angle θ_0 ; the vector potential of Eq.(2) yields

$$\underline{A}_{\text{wire},i}(\underline{r}, t) = \frac{\mu_0}{4\pi} \underline{i}_{\underline{r},i} \int_0^\infty \frac{I_{\text{wire},i}(t - (s + R_i)/c_0)}{R_i} \, ds, \quad (10)$$

where $\underline{i}_{\underline{r},i}$ is the unit tangent along the wire (see Figure A.1), and $I_{\text{wire},i}(t)$ the current in the wire. Furthermore, along the wire we have $R_i = |\underline{r} - (\underline{s}_0 + s \underline{i}_{\underline{r},i})|$, with $0 \leq s \leq \infty$. The unit tangent of the wire is given by

$$\underline{i}_{\underline{r},i} = \cos\varphi_i \cos\theta_0 \underline{i}_x + \sin\varphi_i \underline{i}_y + \cos\varphi_i \sin\theta_0 \underline{i}_z. \quad (11)$$

If the number of wires of the wire mesh to approximate the solid plate is denoted by N , then

$$\begin{aligned}\varphi_i &= (i - \frac{1}{2})\Delta\varphi - \varphi_0, & i=1,2,\dots,N \\ \Delta\varphi &= \frac{2\varphi_0}{N},\end{aligned}\tag{12}$$

where we have assumed that the wires are equidistantly separated by $\Delta\varphi$.

Finally, the total vector potential of a conical wire-mesh wave launcher is given by

$$\underline{A}_{\text{mesh}}(\underline{r}, t) = \sum_{i=1}^N \underline{A}_{\text{wire},i}(\underline{r}, t) = \frac{\mu_0}{4\pi} \sum_{i=1}^N \underline{i}_{\rightarrow,i} \int_0^\infty \frac{I_{\text{wire},i}(t - (s + R_i)/c_0)}{R_i} ds.\tag{13}$$

Comparison Between a Conical-Plate and a Conical Wire-Mesh Wave Launcher:

If the solid plate is subdivided into N small and equidistant current filaments with their centers at φ_i , where N is sufficiently large, then the vector potential of one such a current filament is given by

$$\underline{A}_{\text{plate},i}(\underline{r}, t) = \frac{\mu_0}{4\pi} \int_0^\infty \int_{\varphi_i - \Delta\varphi/2}^{\varphi_i + \Delta\varphi/2} \underline{i}_{\rightarrow} F(\varphi, \varphi_0) \frac{I_0(t - (\rho + R)/c_0)}{R} d\varphi d\rho,\tag{14}$$

where I_0 denotes the total current injected at the plate's apex. After taking all the terms of the integrand of Eq.(14) except $F(\varphi, \varphi_0)$ outside the integral with respect to φ , we get

$$\underline{A}_{\text{plate},i}(\underline{r}, t) \approx \frac{\mu_0}{4\pi} \underline{i}_{\rightarrow,i} \int_0^\infty \frac{I_0(t - (\rho + R_i)/c_0)}{R_i} \int_{\varphi_i - \Delta\varphi/2}^{\varphi_i + \Delta\varphi/2} F(\varphi, \varphi_0) d\varphi d\rho + O(\Delta\varphi^2),\tag{15}$$

where $\underline{i}_{\rightarrow,i}$ is given by Eq.(11). The latter approximation is of second-order accuracy in $\Delta\varphi$.

A direct comparison of Eq.(15) with Eq.(10) shows that the contribution of a current filament of the conical plate equals the contribution of a wire at the center of that filament to second-order accuracy in $\Delta\varphi$, if the following relation holds

$$I_{\text{wire},i}(t) = \int_{\varphi_i - \Delta\varphi/2}^{\varphi_i + \Delta\varphi/2} F(\varphi, \varphi_0) d\varphi I_0(t).\tag{16}$$

In this section, it was shown that if a sufficient number of wires are being used, a conical-plate wave launcher can be approximated by a wire mesh. In the context of this paper, an even more important conclusion based on reciprocity is, that because the conical wire-mesh wave launcher has (almost) the same electromagnetic properties as a conical-plate wave launcher, the current in each wire can be found from the conical-plate current distribution according to Eq.(16).

2.3 Effects not Taken into Account by Our Model

Now that the current's amplitude and waveform are known in the wires, the transient electromagnetic fields are readily obtained with the expressions presented in Appendix A. These expressions are efficient, analytical time-domain expressions for the electromagnetic fields emitted by

a single wire. The total field generated by the simulator is obtained by simply adding the individual contributions of the wires that make up the simulator.

Usually with bounded-wave simulators, a ground plane is provided, which is simply taken into account by using image theory. I.e., with each wire we associate an image wire mirrored in the ground plane. The image wire supports a current that has an opposite sign to the current of the original wire.

The outlined procedure reduces the complexity of the problem dramatically, but the majority of the important mechanisms that contribute to the generated fields are incorporated in this model. The following effects, however, are not taken into account:

- 1 geometry of the wave-launcher/pulser interface,
- 2 additional currents induced in the wires of the upper-plate wire netting and/or the terminating taper when the field generated by the wave launcher strikes these wires (in our model the current in each wire is assumed to have the same waveform and amplitude from pulser to terminator),
- 3 electrical loss in the wires,
- 4 mismatch between the characteristic impedance of the simulator and the terminator,
- 5 geometry of the terminator (the terminator has certain finite dimensions),
- 6 imperfections of the ground plane (in our model the ground plane is assumed to be perfectly conductive and of infinite extent).

From these, the above effects 1 and 2 are the most important ones not incorporated in our model. Note that the effects 2, 4, and 5 are noticeable in the late-time response only.

3 VALIDATION OF THE METHOD OF SOLUTION

Since we have made some assumptions about the current distribution in the wires of the wave launcher (see Section 2.2 for details), it is of paramount importance to check the validity of these assumptions.

Bardet *et al.* [8] computed the current distribution of the wires in the wave launcher of a PPS with the time-domain MoM. This enables us to compare the simple approximation of the TEM-mode current distribution of a conical plate that is presented in Section 2.2 (Eq.(8)).

Figure 2 shows the normalized peak current in the wires of a wave launcher made up of 6, 12 and 18 wires. The even numbered lines are the results of Bardet, while the odd numbered lines show the current in the wires according to our method (Eq.(16)).

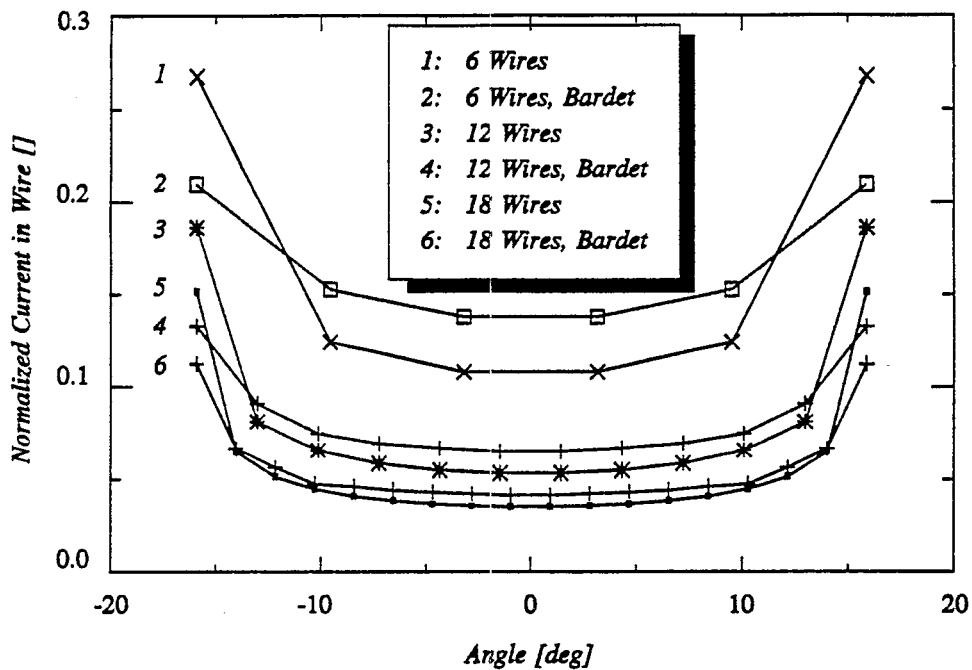


Figure 2 Comparison of the normalized peak currents in the wires of a wave launcher obtained with the MoM solution (Bardet), and from the TEM-mode current distribution of a conical-plate wave launcher (15.9° apex half-angle).

For the six-wire simulator, the simple approximation of Eq.(8) overestimates the current in the outer wires, while it underestimates the current in the wires at the center of the wave launcher. But the more wires one chooses, the better the results one attains. Hence, the currents in a conical wire-mesh wave launcher resemble the current distribution of the TEM-mode supported by a conical-plate wave launcher, as long as enough wires are being used.

Therefore, for a sufficiently large number of wires, the amplitude of the current in each wire can be set equal to the total current in an equivalent TEM-mode current filament of a conical-plate wave launcher. This property has been derived mathematically in Section 2.2.

The wave launcher of a NEMP simulator plays a vital role in the generation of the fields within the working volume (King [12]). It is entirely responsible for the early-time field within the working volume as long as the point of observation is not too close to the upper wire netting. In fact, only a small part of the wave launcher contributes to the first few nanoseconds of the direct wave for points of observations close to the ground plane. This property can be proven from Eq.(A.17) in Appendix A. The contributions of the parallel-plate section and the terminating taper always arrive later than the direct wave from the wave launcher.

The early-time fields emitted by the wave launcher can be obtained from the field expressions of an individual wire, which are presented in Appendix A. In Eq.(A.25), the terms involving R_L vanish for the early time. As each wire of the wave launcher has an image wire with an oppositely directed current, it follows that the term involving $q(t - R_0/c_0)$ is cancelled by the image-wire contribution. Thus the terms involving the current waveform in the wire are the single remaining contributions, i.e.,

$$\underline{E}_i(\underline{r}, t) = - \left\{ \frac{i_{\underline{x},i} - \frac{R_0}{c_0} (\dot{i}_{\underline{x},i} \cdot \underline{R}_0^0)}{1 - \dot{i}_{\underline{x},i} \cdot \underline{R}_0^0} - \frac{i_{\underline{x},i}^* - \frac{R_0}{c_0} (\dot{i}_{\underline{x},i}^* \cdot \underline{R}_0^0)}{1 - \dot{i}_{\underline{x},i}^* \cdot \underline{R}_0^0} \right\} \frac{Z_0 I_{wire,i}(t - R_0/c_0)}{4\pi R_0}, \quad t < \frac{L + R_L}{c_0} \quad (17)$$

where for the wave launcher $i_{\underline{x},i}$ is given by Eq.(11), and the quantities that are reflected at the x, y plane are denoted by the superscript asterisk. Thus (cf. Eq.(11)),

$$i_{\underline{x},i}^* = \cos\varphi_i \cos\theta_0 i_{\underline{x}} + \sin\varphi_i i_{\underline{y}} - \cos\varphi_i \sin\theta_0 i_{\underline{z}}. \quad (18)$$

Since the current's argument does not have any φ dependency, the total early-time electric field of the conical wire-mesh wave launcher is given by

$$\begin{aligned} \underline{E}(\underline{r}, t) = & - \frac{Z_0 I_0(t - R_0/c_0)}{4\pi R_0} \sum_{i=1}^N \left\{ \frac{i_{\underline{x},i} - \frac{R_0}{c_0} (\dot{i}_{\underline{x},i} \cdot \underline{R}_0^0)}{1 - \dot{i}_{\underline{x},i} \cdot \underline{R}_0^0} \right. \\ & \left. - \frac{i_{\underline{x},i}^* - \frac{R_0}{c_0} (\dot{i}_{\underline{x},i}^* \cdot \underline{R}_0^0)}{1 - \dot{i}_{\underline{x},i}^* \cdot \underline{R}_0^0} \right\} \int_{\varphi_i - \Delta\varphi/2}^{\varphi_i + \Delta\varphi/2} F(\varphi, \frac{N}{N-1} \varphi_a) d\varphi, \end{aligned} \quad (19)$$

where we have used Eq.(16), and where I_0 denotes the current delivered by the pulser. Observe that φ_a denotes the apex half-angle of the conical wire-mesh wave launcher, and is given by $\varphi_a = \frac{N-1}{N} \varphi_0$. Therefore, in terms of φ_a

$$\begin{aligned} \varphi_i &= (i-1)\Delta\varphi - \varphi_a, & i &= 1, 2, \dots, N \\ \Delta\varphi &= \frac{2\varphi_a}{N-1}, \end{aligned} \quad (20)$$

Eq.(19) shows that the waveform of the early-time field exactly equals the current waveform delivered by the pulser.

If the point of observation is located on the ground plane and along the center line of the

simulator ($y = 0, z = 0$), Eq.(19) further reduces to

$$\underline{E}(r, t) = -\frac{Z_0 I_0(t-R_0/c_0)}{2\pi R_0} \underline{i}_z \sum_{i=1}^N \frac{\cos\varphi_i \sin\theta_0}{1 - \cos\varphi_i \cos\theta_0} \int_{\varphi_i-\Delta\varphi/2}^{\varphi_i+\Delta\varphi/2} F(\varphi, \frac{N}{N-1} \varphi_a) d\varphi. \quad (21)$$

Note that the term in the summation is independent of the point of observation, so that in this case the field emitted by the wave launcher exhibits the expected $1/R_0$ dependence.

The early-time electric field of Eq.(19) enables us to derive an analytical expression for the wave-launcher's (early-time) characteristic impedance, which can be found from

$$Z = \frac{\lim_{R_0 \rightarrow 0} -\int_C \underline{E} \cdot d\underline{l}}{I_0} = \frac{\lim_{R_0 \rightarrow 0} -\int_0^{\theta_0} \underline{i}_\theta \cdot \underline{E} R_0 d\theta}{I_0}, \quad (22)$$

where the path of integration C is chosen as an arc in the x, z -plane from the ground plane to the upper plate. Therefore along C , \underline{R}_0^0 and \underline{i}_θ are given by

$$\begin{aligned} \underline{R}_0^0 &= \cos\theta \underline{i}_x + \sin\theta \underline{i}_z, \\ \underline{i}_\theta &= -\sin\theta \underline{i}_x + \cos\theta \underline{i}_z. \end{aligned} \quad (23)$$

Note that \underline{R}_0^0 and \underline{i}_θ are perpendicular along C . After some simple algebraic manipulation, the impedance of a conical wire-mesh wave launcher given by Eq.(22) is then readily obtained as

$$Z = \frac{Z_0}{4\pi} \sum_{i=1}^N \ln \frac{1 - \cos\varphi_i \cos 2\theta_0}{1 - \cos\varphi_i} \int_{\varphi_i-\Delta\varphi/2}^{\varphi_i+\Delta\varphi/2} F(\varphi, \frac{N}{N-1} \varphi_a) d\varphi. \quad (24)$$

Observe that this expression has a singularity at $\varphi_i = 0$. This singularity is due to the assumption that the wires are infinitely thin. Without loss of generality, this singularity can be circumvented by allowing even values for N only.

Without proof we give the impedance of the conical-plate wave launcher, which can be derived in a similar manner,

$$Z = \frac{Z_0}{2\pi} \int_0^{\varphi_0} \ln \frac{1 - \cos\varphi \cos 2\theta_0}{1 - \cos\varphi} F(\varphi, \varphi_0) d\varphi. \quad (25)$$

This expression has singularities at the integration-interval end points, which are integrable. A plot of the characteristic impedance of the conical-plate wave launcher as a function of the apex half-angle φ_0 is depicted in Figure 3. Similar plots can readily be obtained for the conical wire-mesh wave launcher from Eq.(24).

An important property can be obtained from Eq.(24) and (25): the characteristic impedance of the conical wire-mesh wave launcher with apex half-angle φ_a can approximately be obtained from the characteristic impedance of a conical-plate wave launcher with apex half-angle $\frac{N}{N-1} \varphi_a$.

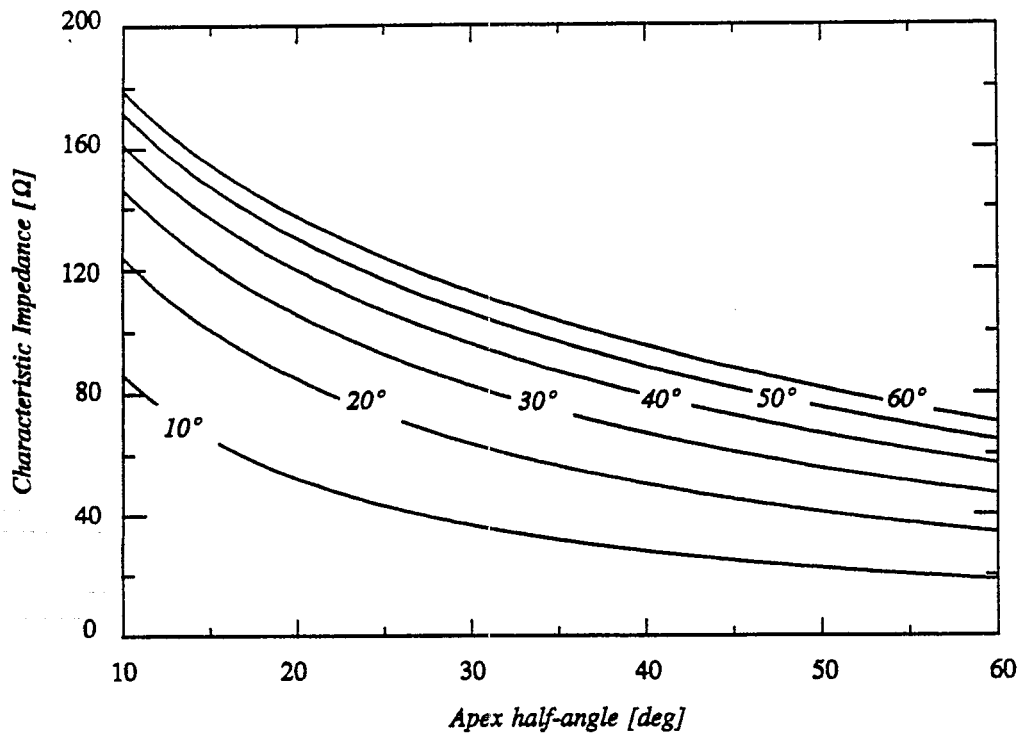


Figure 3 Characteristic impedance of a conical-plate wave launcher as a function of the apex-half-angle ϕ_0 with the elevation angle θ_0 as parameter.

5 COMPARISON OF SOME RESULTS WITH MEASUREMENTS

The method developed was implemented in a computer program called WS. We have used the WS code to predict the fields of some full-scale experimental simulators that were built by TNO (Pont [14]) for research purposes. Unfortunately, these temporary experimental simulators were not terminated properly, which resulted in a mismatch between the characteristic impedance of the transmission lines and the terminator. For more details the reader is referred to [14].

We have matched the pulser waveform with a double-exponential waveform as close as possible, and have used this for the current waveform in the wires. Figure 4 shows the field in a PPS (cf. Figure 15a of [14]), and Figure 5 in a Triangular-Plate Simulator (TPS) (cf. Figure 16a of [14])³.

The signals are scaled in amplitude in such away that the first peaks of the signals have equal amplitude. Both measurements show repeated reflections, which are probably due to the mismatch between the characteristic impedance of the transmission lines and the terminator. Especially the results of the TPS match very well.

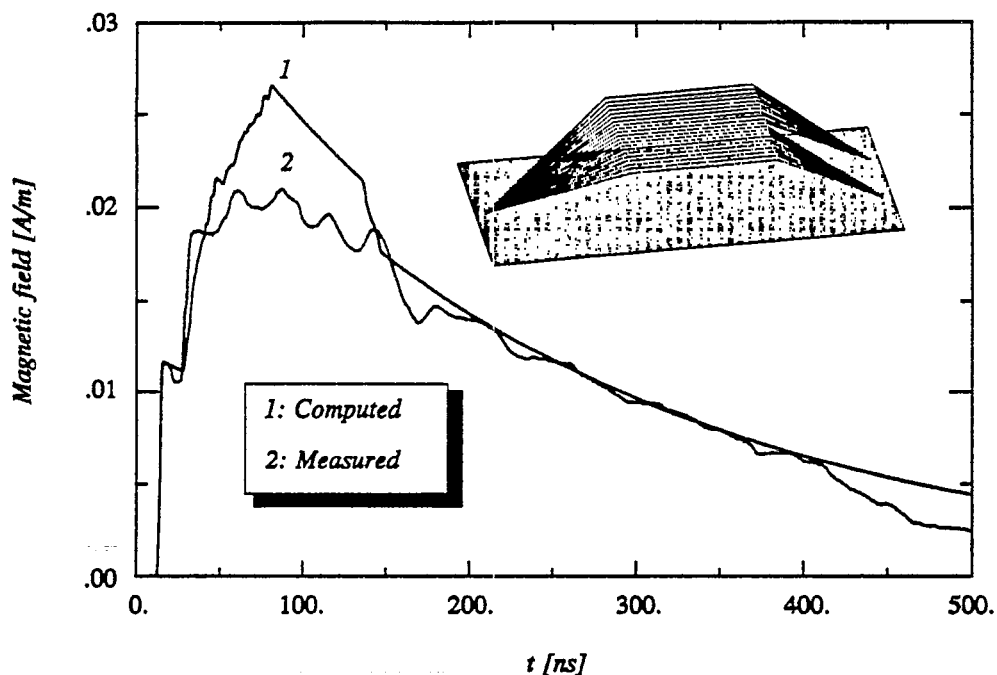


Figure 4 Comparison of measured and computed horizontal component of the magnetic field in a PPS.

³The measurements presented in this report were compensated for sensor droop, whereas the measurements presented in Pont [14] were not.

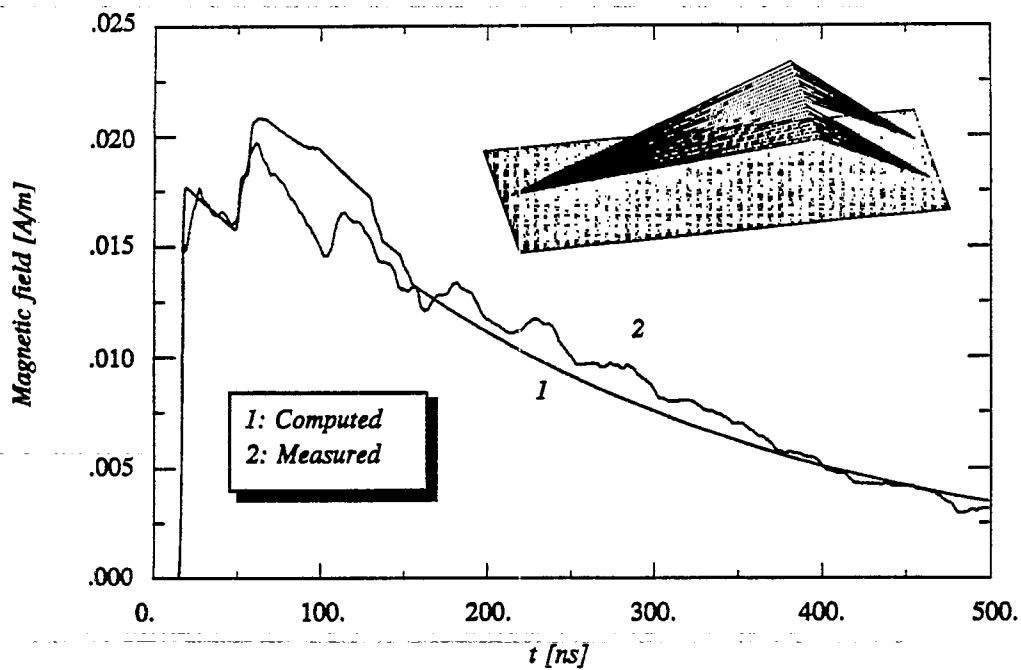


Figure 5 Comparison of measured and computed horizontal component of the magnetic field in a TPS.

Performance of the WS code

On a PC with a 33 MHz 80486 CPU, for one observation point the outlined method takes about 83 μ s for one wire per time step. For a 75-wire TPS and say 200 time steps, the time required is about 5 seconds.

As mentioned in the introduction, the WS program has been developed and used for the electromagnetic-performance analysis of the reference design of EMPSIS (Klaasen *et al.* [1]). EMPSIS is the result of a feasibility study into a simulator that can accommodate large naval vessels. It is a draw-board TPS suspended over sea water. The outline of EMPSIS is depicted in Figure 6. Some results obtained for EMPSIS will be presented here to illustrate our method.

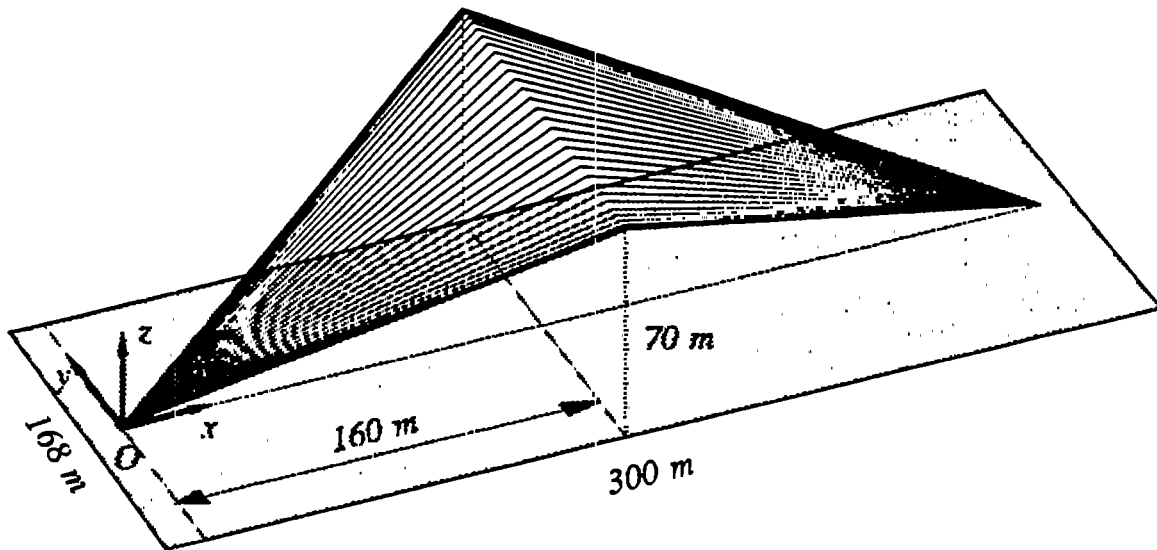


Figure 6 Outline of EMPSIS. Wave-launcher elevation angle $\theta_0 = 23.6^\circ$, apex half-angle $\phi_a = 25.7^\circ$.

The working volume starts at 125 m from the wave-launcher's apex, and the working-volume's center is located at $\underline{r} = (142.5, 0, 0)^4$.

6.1 Calculation of the Characteristic Impedance of EMPSIS

The (early-time) characteristic impedance can be computed by the WS code by determining the total peak current injected in the wave-launcher's apex that is required to generate the threat-level field within the working volume, but it is easier to use the analytical expression of Eq.(24) of Chapter 4.

Table I lists the characteristic impedance for different numbers of wires. In the second column the values are obtained from Eq.(24). The values in the third column are obtained from the conical-

⁴ See Figure 6 for a definition of the coordinate system used. The origin of the coordinate system coincides with the pulser's location.

plate wave-launcher impedance given by Eq.(25) with $\varphi_0 = \frac{N}{N-1} \varphi_a$.

Table I Characteristic impedance of EMPSIS as a function of the number of wires.

Number of Wires N	Characteristic Impedance [Ω]	Approximated Characteristic Impedance [Ω]
10	72.2	73.9
18	75.5	76.4
30	77.1	77.7
76	78.7	78.8

It clearly shows that, although the characteristic impedance of the simulator depends on the number of wires, the differences are small.

6.2 The Electromagnetic-Performance Analysis of EMPSIS

The field within the working volume is not homogeneous, especially close to the upper wire netting and its edges. Therefore, we analyze the field distribution within the working volume in this section with the method described in Chapter 2.

So far, we have seen that the number of wires does not have a significant influence on the characteristic impedance of the simulator, but one expects some pronounced field enhancements within the upper part of the working volume.

We consider the peak field distribution at the working-volume center ($x = 142.5 \text{ m}$) as a function of the height to study the field enhancements in the proximity of the wire netting. The Figures 7 - 8 show the results at the working-volume center in the transverse direction. Because the differences are small, we only show the cases for 18 and 75 wires. The peak electric field has been normalized with the peak electric field at ground level in the working-volume center, i.e., at $\underline{r} = (142.5, 0, 0)$.

Both figures show that the peak field strength at ground level underneath the outer edge of the wire netting ($y = 75 \text{ m}$) reduces to 75% of the peak field strength at the working-volume center. At the far end of the working volume ($y = 100 \text{ m}$), the peak field strength reduces to 60% of the peak field strength at the working-volume center.

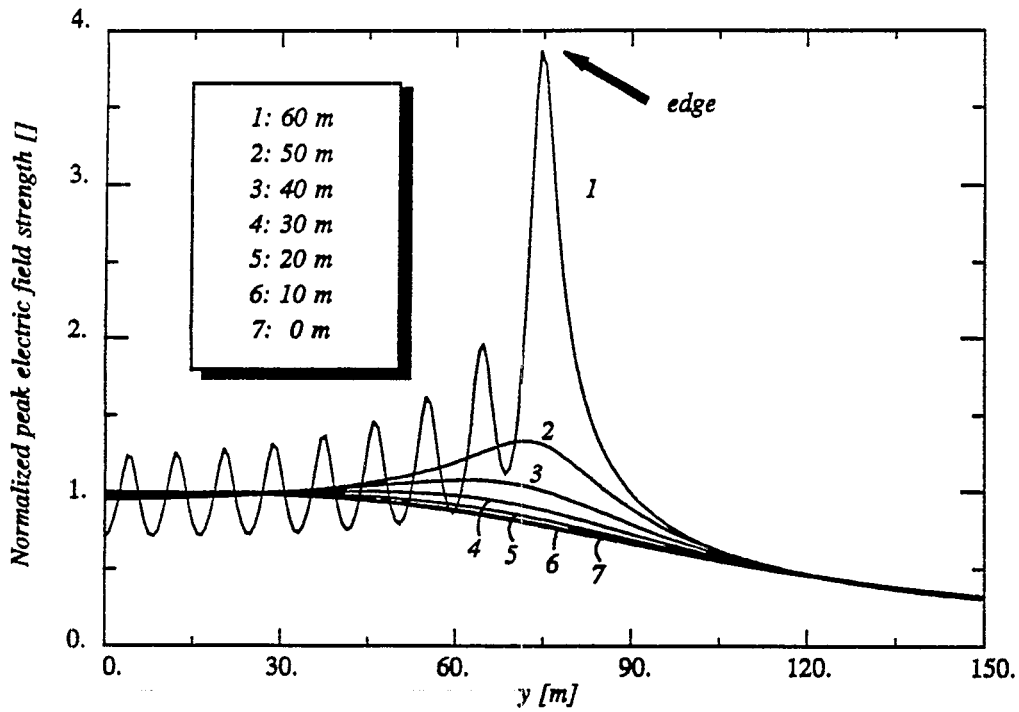


Figure 7 The normalized peak electric field strength at the working-volume center ($x = 142.5$ m) in the transverse direction, 18 wires.

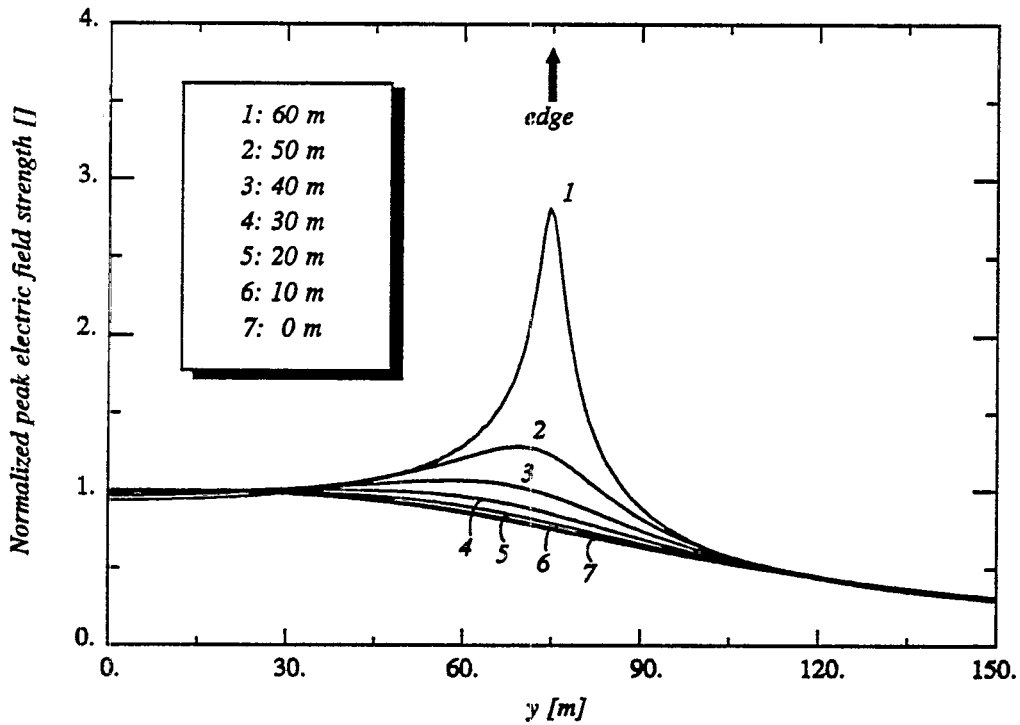


Figure 8 The normalized peak electric field strength at the working-volume center ($x = 142.5$ m) in the transverse direction, 75 wires.

All the previous results in this chapter were obtained from the early-time peak field strength of the direct wave when no spurious reflections yet occur. But as soon as the currents in the wave-

launcher wires flow into the terminating-taper wires, reflections can be observed in the generated fields. This is illustrated in Figures 9 - 11, where the simulator is made up of 18, 31 and 75 wires, respectively. As current waveform we have used the following double-exponential waveform

$$I(t) = I_0(e^{-\alpha t} - e^{-\beta t}), \quad (26)$$

with

$$\begin{aligned} \alpha &= 3.705 \times 10^6 \text{ [s}^{-1}\text{]}, \\ \beta &= 3.908 \times 10^8 \text{ [s}^{-1}\text{]}. \end{aligned} \quad (27)$$

I_0 has been chosen so that the peak field strength at $\underline{r} = (142.5, 0, 0)$ equals 50 kV/m.

The first reflection occurs at different points in time (the so-called clear time) depending on the height of the observation point. This is due to the terminating-taper wire nearest to the point of observation. The clear time for EMPSIS is always larger than 142 ns within the working volume⁵. Subsequent reflections can be identified which are due to the outer terminating-taper wires.

A comparison of Figures 9 - 11 shows that the number of wires does not effect the (early time) direct wave (much) within the working volume. In the late time, the individual (discrete) contribution of each wire in Figures 9 and 10 is noticeable. As has been pointed out in Chapter 4, the early-time field exactly equals the current waveform.

⁵ The minimum clear time in the working volume occurs at the point $\underline{r} = (150, 0, 47)$.

Figure 9 Electric field at the working-volume center ($x = 142.5 \text{ m}$) as a function of time [ns], 18 wires. 1: x-component, 2: y-component, 3: z-component.

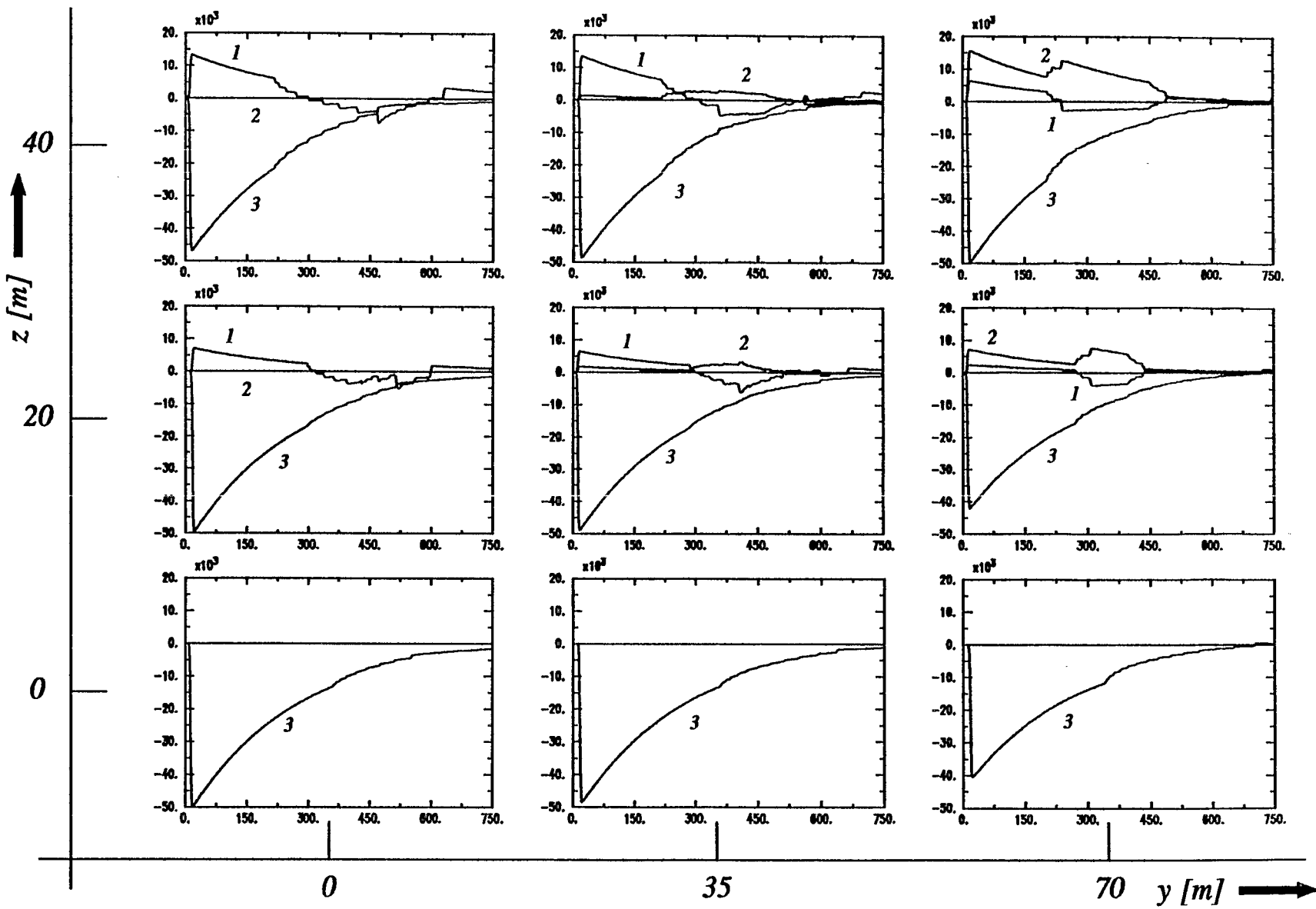


Figure 10 Electric field at the working-volume center ($x = 142.5 \text{ m}$) as a function of time [ns], 31 wires, 1: x-component, 2: y-component, 3: z-component.

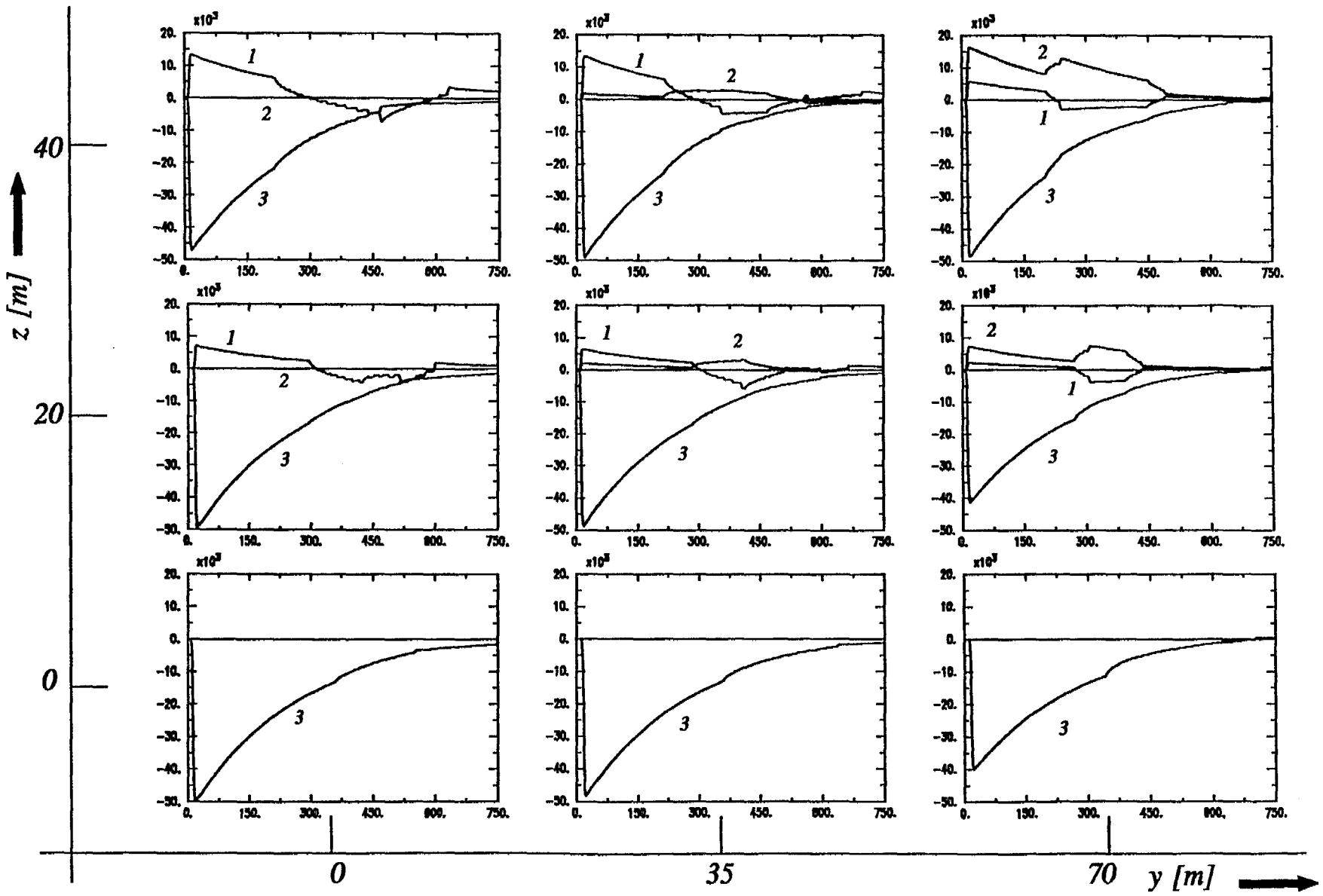
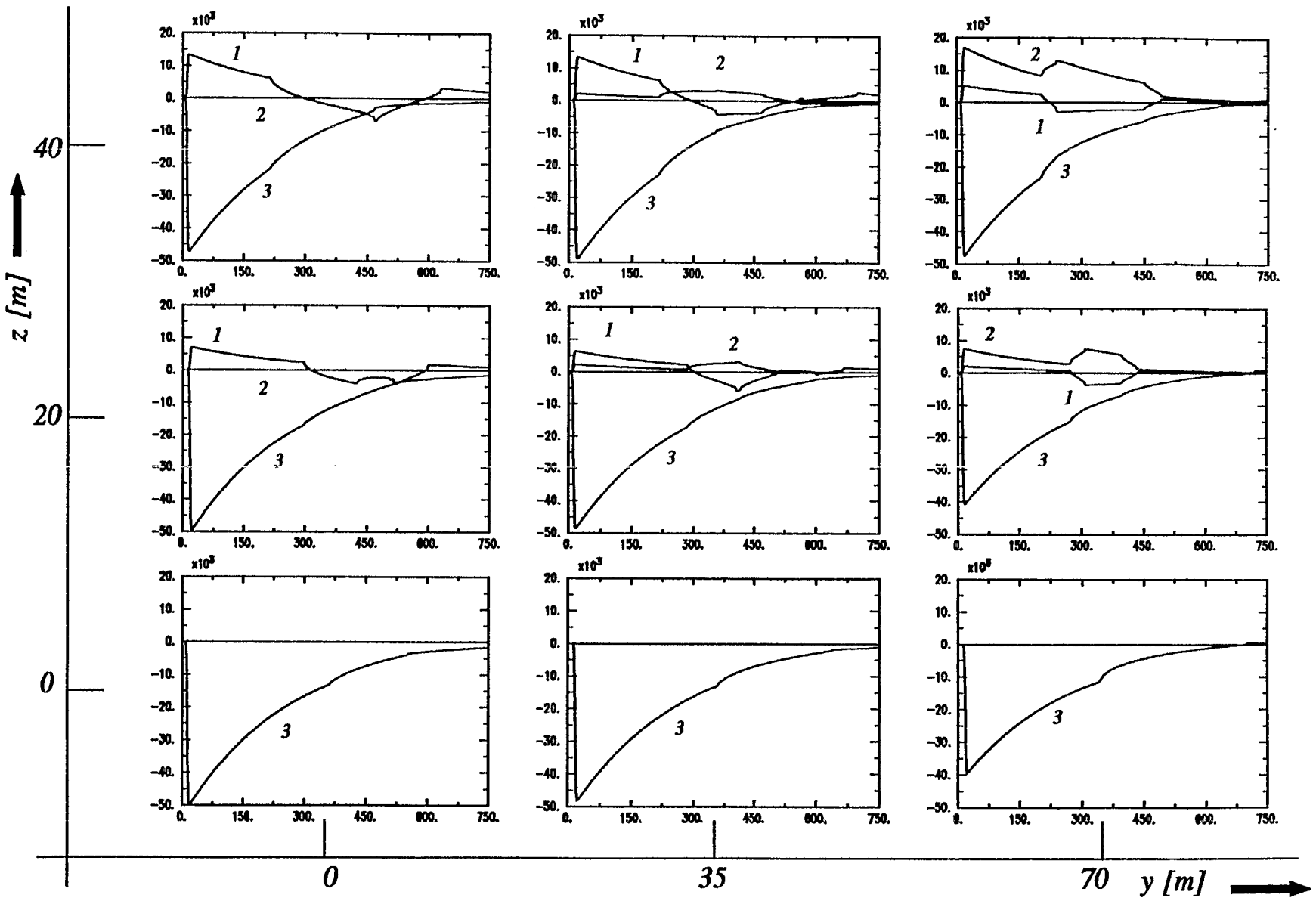


Figure 11 Electric field at the working-volume center ($x = 142.5 \text{ m}$) as a function of time [ns], 75 wires, 1: x-component, 2: y-component, 3: z-component.



Finally, we have computed the electric field strength within the simulator and its vicinity at ground level. The results are depicted in Figure 12, and were obtained with the same method as described in Chapter 2, but were calculated with the *Mathematica* program [15], which does the contour plotting. The simulator was modelled with only 15 wires, otherwise the *Mathematica* program takes too long to compute the results. A gain, the peak field strength at the simulator's center has been set to 50 kV/m.

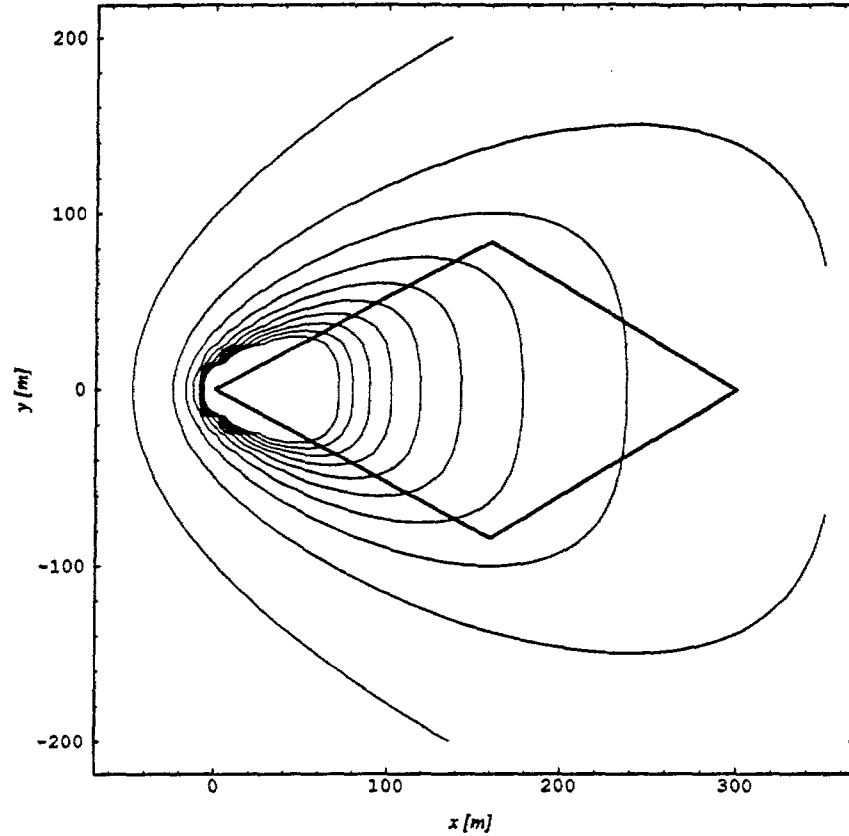


Figure 12 Peak electric field strength at ground level within and in the vicinity of the simulator (wave launcher only). The contours range from 10 kV/m to 100 kV/m with 10 kV/m increments (inner contours correspond with higher levels).

Furthermore, we did not take into account the contribution of the terminating taper. The actual expression which was used is Eq.(18). Near the wave launcher, the contribution of the terminating taper can be neglected since it occurs in the late time and thus does not affect the peak field strength.

Since the terminating taper has almost the same dimensions as the wave launcher, it exhibits the same behavior as the wave launcher, i.e., Figure 12 can also be used for the electric fields within and in the vicinity of the terminating taper.

For completeness, Figure 13 shows an electric field mapping on a larger scale.

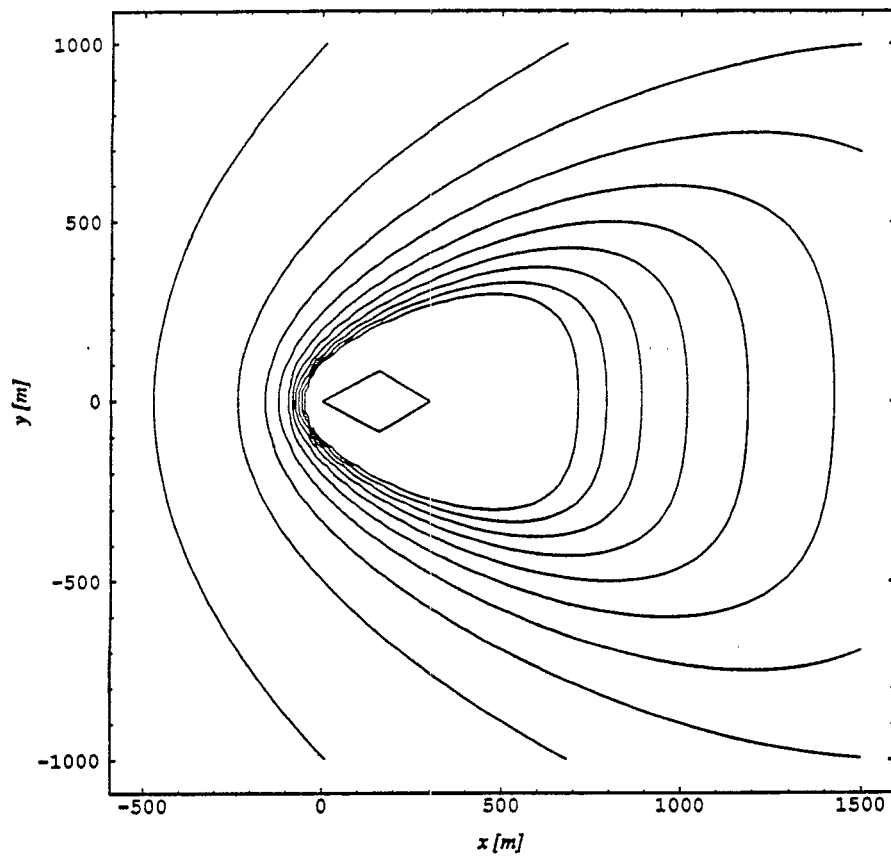


Figure 13 Peak electric field strength at ground level outside the simulator (wave launcher only). The contours range from 1 kV/m to 10 kV/m with 1 kV/m increments (inner contours correspond with higher levels).

7 CONCLUSIONS

The method developed has proven to be useful, and has increased the understanding and interpreting of the fields generated by a NEMP simulator. In particular, we have derived expressions for the important early-time fields generated by the simulator, from which the characteristic impedance of a conical-plate wave launcher and the conical wire-mesh wave launcher have been derived. It was found that if a sufficient number of wires are being used, the working-volume fields emitted by a conical wire-mesh wave launcher behave like those of a conical-plate wave launcher. The resemblance breaks down for points of observation close to the wire-netting. The early-time fields emitted by the conical wire-mesh wave launcher have the same waveform as the current delivered by the source (the pulser).

The method can be extended and improved in the following manners:

- 1 use a more accurate representation of the current distribution of the TEM-mode in a conical-plate wave launcher (more research needed),
- 2 include the additional currents induced in the wires of the upper-plate wire netting and/or the terminating taper when the field generated by the wave launcher strikes these wires (at the expense of an increase of the computational time, but still far less than the time-domain MoM),
- 3 take into account the electrical loss in the wires (may explain the height-dependent rise time observed in experiments [17], p.19),
- 4 model the mismatch between the characteristic impedance of the simulator and the terminator.

In addition, if the method developed is extended so that ground reflections are taken into account, it can also be used to assess the radiated fields far away from ground-based simulators.

The program developed (WS code) is very efficient, and very valuable from an engineering point of view: changes in the design of a NEMP simulator can rapidly be evaluated.

ACKNOWLEDGEMENT

The author wishes to thank W. Pont of TNO-FEL and R.R. Klompenhouwer of DMKM/PFS for their support and encouragement.

REFERENCES

- [1] Klaasen, J.J.A., W., Pont, A.B., Woltering, C.D. de Haan, Design of a Nuclear EMP simulator for Ships (EMPSIS), *TNO-FEL report: FEL-92-A245*, August 1992.
- [2] Baum, C.E., Impedances and Field Distributions for Parallel Plate Transmission Line Simulators, *Sensor and Simulation Notes*, Note 11, 6 June 1966, pp. 27 - 31.
- [3] Giri, D.V., T.K. Liu, F.M. Tesche, R.W.P. King, Parallel Plate Transmission Line Type of EMP Simulators: A Systematic Review and Recommendations, *Sensor and Simulations Notes*, Note 261, 1 April 1980, pp. 80 - 97.
- [4] Harrington, R.F., Field Computation by Moment Methods, The Macmillan Company, 1968.
- [5] Mittra (editor), R., Numerical and Asymptotic Techniques in Electromagnetics, in *Topics in Applied Physics Volume 3*, Springer-Verlag, 1975.
- [6] Burke, G.J., A.J. Poggio, Numerical Electromagnetic Code (NEC) - Method of Moments, Part III: User's Guide, January 1981, Lawrence Livermore National Laboratory.
- [7] De Haan, C.D., W. Pont, M.A. Ouwens, Feasibility study of a NEMP simulator for ships (EMPSIS). Theoretical analysis and experiments, *TNO-FEL report: FEL-91-B249*, September 1991.
- [8] Bardet, C., O. Dafif, B. Jecko, "Time-Domain Analysis of a Large EMP Simulator," *IEEE Transactions on Electromagnetic Compatibility*, Vol. EMC-29, No. 1, February 1987, pp. 40 - 48.
- [9] Dafif, O., C. Bardet, B. Jecko, "Transient Field Distribution in a Transmission Line Simulator," *EMC Symposium & Exhibition*, Zurich 1985, pp. 359 - 363.
- [10] Nuclear survivability criteria for armed forces material and installations, Allied Engineering Publication AEP-4, Annex A, Edition 4, August 1990, NATO SECRET.
- [11] King, R.W.P., *et al.*, "Theoretical Analysis of the Rhombic Simulator Under Pulse Excitation," *IEEE Transactions on Electromagnetic Compatibility*, Vol. EMC-25, No. 1, February 1983, pp. 47 - 55.
- [12] King, R.W.P., *et al.*, "The Exciting Mechanism of the Parallel-Plate EMP Simulator," *IEEE Transactions on Electromagnetic Compatibility*, Vol. EMC-29, No. 1, February 1987, pp. 32 - 39.
- [13] Giri, D.V., Terminator Design for Sapiens-II, *SAPIENS Memos*, Memo 12, December 1990.
- [14] Pont, W., NEMP-simulator shape experiments, Magnetic Field Measurements in a Parallel-Plate Line and in a Continuous Taper Line, *TNO-FEL report: FEL-91-A303*, November 1991, Confidential.
- [15] *Mathematica*, A System for Doing Mathematics by Computer, Second Edition, Addison-Wesley Publishing Company, Inc.
- [16] Jones, D.S., The Theory of Electromagnetism, Pergamon Press, 1964, p. 144.
- [17] Rothwell, E.J., *et al.*, "Transient Field Produced by a Traveling-Wave Wire Antenna," *IEEE Transactions on EMC*, VOL. 33, NO. 3, August 1991, pp. 172 - 178.

A THE TRANSIENT ELECTROMAGNETIC FIELDS EMITTED BY A CURRENT-CARRYING STRAIGHT WIRE

A.1 Formulation of the Problem

This appendix concerns the transient electromagnetic fields emitted by a current-carrying straight wire. The derivation is based on the Liénard-Wiechert potentials for a wire (Jones [16]), and on Rothwell's work [17]. The wire is uncoated, and made of perfectly conducting material. The current in the wire is assumed to be known, and propagates with speed c_0 (the speed of light) along the wire. Exact, analytical expressions are derived, which give a dramatic reduction of the computational time compared with the method described by King [11].

The position vector in a orthogonal right-handed Cartesian reference frame is given by

$$\underline{r} = x\underline{i}_x + y\underline{i}_y + z\underline{i}_z, \quad (\text{A.1})$$

with unit vectors \underline{i}_x , \underline{i}_y and \underline{i}_z . The vector potential in this reference frame due to an arbitrary current source is given by

$$\underline{A}(\underline{r}, t) = \frac{\mu_0}{4\pi} \int_V \frac{\underline{J}(t-R/c_0, \underline{r}')}{R} dV(\underline{r}'), \quad (\text{A.2})$$

where \underline{J} denotes the current volume density, and $R = |\underline{R}| = |\underline{r} - \underline{r}'|$.

The electric field is readily obtained from

$$\underline{E}(\underline{r}, t) = -\underline{\nabla}\phi(\underline{r}, t) - \partial_t \underline{A}(\underline{r}, t), \quad (\text{A.3})$$

where ϕ denotes the scalar potential given by

$$\phi(\underline{r}, t) = -c_0^2 \underline{\nabla} \cdot \underline{\tilde{A}}(\underline{r}, t). \quad (\text{A.4})$$

In Eq.(A.4), $\underline{\tilde{A}}$ is the time-integrated vector potential.

The magnetic field is simply found from the vector potential in the following way

$$\underline{H}(\underline{r}, t) = \mu_0^{-1} \underline{\nabla} \times \underline{A}(\underline{r}, t). \quad (\text{A.5})$$

For a straight wire the vector potential of Eq.(A.2) is rewritten as

$$\underline{A}(\underline{r}, t) = \frac{\mu_0}{4\pi} \underline{i}_s \int_0^L \frac{I(t-(s+R)/c_0)}{R} ds, \quad (\text{A.6})$$

where \underline{i}_s is the unit tangent along the wire (see Figure A.1), L denotes the length of the wire, and $I(t)$ the current in the wire. Furthermore, along the wire we have $\underline{r}' = \underline{s}_0 + s\underline{i}_s$, with $0 \leq s \leq L$, and where \underline{s}_0 denotes the start of the wire.

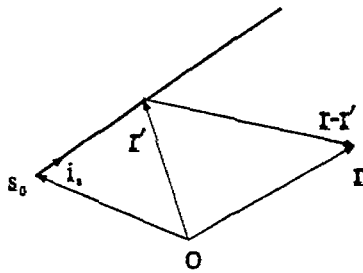


Figure A.1 Current-carrying wire.

The Vector-Potential Impulse Response

The line integral occurring in Eq.(A.6) of the vector potential can be solved by determining the vector-potential impulse response, i.e., by setting $I(t) = \delta(t)$. This yields

$$\underline{A}_i(\underline{r}, t) = \frac{\mu_0}{4\pi} \underline{i}_s \int_0^L \frac{\delta(t - (s+R)/c_0)}{R} ds, \quad (\text{A.7})$$

where the subscript i indicates the impulse response.

After making the change of variable $u = G(s) = t - (s+R)/c_0$, the vector-potential impulse response is calculated as

$$\underline{A}_i(\underline{r}, t) = \frac{Z_0}{4\pi} \underline{i}_s \int_{G(0)}^{G(L)} \frac{\delta(u)}{\underline{i}_s \cdot \underline{R} - R} du, \quad (\text{A.8})$$

where we have used that (note that R depends on s as well)

$$\frac{du}{ds} = \frac{dG(s)}{ds} = \frac{1}{c_0} \left(\underline{i}_s \cdot \frac{\underline{R}}{R} - 1 \right). \quad (\text{A.9})$$

The vector potential is rewritten as

$$\underline{A}_i(\underline{r}, t) = \frac{Z_0}{4\pi} \underline{i}_s \left\{ U\left(t - \frac{L+R_L}{c_0}\right) - U\left(t - \frac{R_0}{c_0}\right) \right\} \lim_{u \rightarrow 0} \frac{1}{\underline{i}_s \cdot \underline{R} - R}, \quad (\text{A.10})$$

where $R_0 = |\underline{R}_0| = |\underline{r} - \underline{s}_0|$, and $R_L = |\underline{R}_L| = |\underline{r} - (\underline{s}_0 + L\underline{i}_s)| = |\underline{R}_0 - L\underline{i}_s|$. In Eq.(A.10), $U(t)$ denotes the Heaviside unit-step function. Note that

$$\lim_{u \rightarrow 0} \frac{1}{\underline{i}_s \cdot \underline{R}(s) - R(s)} = \lim_{u \rightarrow 0} \frac{1}{\underline{i}_s \cdot \underline{R}(G^{-1}(u)) - R(G^{-1}(u))} = \frac{1}{\underline{i}_s \cdot \underline{R}(s_0) - R(s_0)}, \quad (\text{A.11})$$

where $G^{-1}(u)$ follows from the definition of G , and $s_0 = G^{-1}(0)$. Since $t - (s_0 + R(s_0))/c_0 = 0$, we find that $R(s_0) = c_0 t - s_0$. Hence,

$$\underline{i}_s \cdot \underline{R}(s_0) - R(s_0) = \underline{i}_s \cdot (\underline{R}_0 - s_0 \underline{i}_s) - (c_0 t - s_0) = \underline{i}_s \cdot \underline{R}_0 - c_0 t. \quad (\text{A.12})$$

After substituting Eq.(A.12) into Eq.(A.10), we get

$$\underline{A}_i(\underline{r}, t) = \frac{Z_0}{4\pi} \frac{\underline{i}_s}{D} \left\{ U\left(t - \frac{R_0}{c_0}\right) - U\left(t - \frac{L+R_L}{c_0}\right) \right\}, \quad (\text{A.13})$$

with

$$D = c_0 t - \underline{i}_s \cdot \underline{R}_0. \quad (\text{A.14})$$

For completeness, $G^{-1}(u)$ is given by

$$s = G^{-1}(u) = \frac{1}{2} \frac{c_0^2 (t-u)^2 - R_0^2}{c_0 (t-u) - \underline{i}_s \cdot \underline{R}_0}, \quad (\text{A.15})$$

and therefore

$$s_0 = G^{-1}(0) = \frac{1}{2} \frac{c_0^2 t^2 - R_0^2}{c_0 t - \underline{i}_s \cdot \underline{R}_0} = \frac{1}{2} \frac{c_0^2 t^2 - R_0^2}{D}. \quad (\text{A.16})$$

Note that the physical interpretation of s_0 is the segment length that contributes to the field at the point of observation \underline{r} and the point in time t ($t > R_0/c_0$). The segment length that contributes to the field at \underline{r} within a time window t_w after the wavefront has arrived, is given by

$$s_0 = \frac{1}{2} \frac{c_0 t_w (c_0 t_w + 2R_0)}{c_0 t_w + D_0}. \quad (\text{A.17})$$

The Scalar-Potential Impulse Response

The scalar potential ϕ is given by $\phi = -c_0^2 \underline{\nabla} \cdot \underline{\tilde{A}}$, so that the time-integrated vector potential is required. The time-integrated vector potential is given by

$$\underline{\tilde{A}}_i(\underline{r}, t) = \frac{\mu_0}{4\pi} \left\{ (\ln D - \ln D_0) U\left(t - \frac{R_0}{c_0}\right) - (\ln D - \ln D_L) U\left(t - \frac{L+R_L}{c_0}\right) \right\} \underline{i}_s, \quad (\text{A.18})$$

with

$$\begin{aligned} D_0 &= R_0 - \underline{i}_s \cdot \underline{R}_0, \\ D_L &= R_L - \underline{i}_s \cdot \underline{R}_L. \end{aligned} \quad (\text{A.19})$$

The divergence of the time-integrated vector potential is given by

$$\begin{aligned} \underline{\nabla} \cdot \underline{\tilde{A}}_i &= \underline{i}_s \cdot \underline{\nabla} \tilde{A}_i = \frac{\mu_0}{4\pi} \left\{ \left(\frac{1 - \underline{i}_s \cdot \underline{R}_0^0}{D_0} - \frac{1}{D} \right) U\left(t - \frac{R_0}{c_0}\right) \right. \\ &\quad \left. - \left(\frac{1 - \underline{i}_s \cdot \underline{R}_L^0}{D_L} - \frac{1}{D} \right) U\left(t - \frac{L+R_0}{c_0}\right) \right\}, \end{aligned} \quad (\text{A.20})$$

with $\underline{R}_L^0 = \underline{R}_L/R_L$ and $\underline{R}_0^0 = \underline{R}_0/R_0$. In Eq.(A.20), we have used $\underline{\nabla} D = -\underline{i}_s$, and $\underline{\nabla} D_i = \underline{R}_i^0 - \underline{i}_s$ (i takes the values 0 and L). After substituting the expressions for D_L and D_0 given by Eq.(A.19) into Eq.(A.20), we finally find for the scalar-potential impulse response

$$\phi_i(\underline{r}, t) = -\frac{1}{4\pi\epsilon_0} \left\{ \left(\frac{1}{R_0} - \frac{1}{D} \right) U\left(t - \frac{R_0}{c_0}\right) - \left(\frac{1}{R_L} - \frac{1}{D} \right) U\left(t - \frac{L+R_L}{c_0}\right) \right\}. \quad (\text{A.21})$$

Eq.(A.13) and (A.21) are the Liénard-Wiechert potentials for a wire.

The Electric Field

Before the electric field can be determined, $\underline{\nabla}\phi_i$ and $\partial_t \underline{A}_i$ have to be derived first from Eq.(A.21) and Eq.(A.13), respectively. Therefore,

$$\begin{aligned} \underline{\nabla}\phi_i = \frac{1}{4\pi\epsilon_0} \left\{ \left(\frac{\underline{i}_s}{D^2} + \frac{R_0^0}{R_0^2} \right) U\left(t - \frac{R_0}{c_0}\right) - \left(\frac{\underline{i}_s}{D^2} + \frac{R_L^0}{R_L^2} \right) U\left(t - \frac{L+R_L}{c_0}\right) \right. \\ \left. - c_0^{-1} \frac{\underline{i}_s \cdot R_0^0}{D_0} R_0^0 \delta\left(t - \frac{R_0}{c_0}\right) + c_0^{-1} \frac{\underline{i}_s \cdot R_L^0}{D_L} R_L^0 \delta\left(t - \frac{L+R_L}{c_0}\right) \right\}, \end{aligned} \quad (\text{A.22})$$

where we have used $\underline{\nabla}R_i = \frac{R_i^0}{R_i}$.

The time derivative of the vector potential follows from Eq.(A.13). It is given by

$$\begin{aligned} \partial_t \underline{A}_i(\underline{r}, t) = -\frac{Z_0}{4\pi} \left\{ \frac{c_0}{D^2} \left[U\left(t - \frac{R_0}{c_0}\right) - U\left(t - \frac{L+R_L}{c_0}\right) \right] \right. \\ \left. - \frac{1}{D_0} \delta\left(t - \frac{R_0}{c_0}\right) + \frac{1}{D_L} \delta\left(t - \frac{L+R_L}{c_0}\right) \right\} \underline{i}_s, \end{aligned} \quad (\text{A.23})$$

so that the electric-field impulse response is given by

$$\begin{aligned} \underline{E}_i(\underline{r}, t) = -\frac{1}{4\pi\epsilon_0} \left\{ \frac{R_0^0}{R_0^2} U\left(t - \frac{R_0}{c_0}\right) + c_0^{-1} \left(\frac{\underline{i}_s \cdot R_0^0 (\underline{i}_s \cdot R_0^0)}{D_0} \right) \delta\left(t - \frac{R_0}{c_0}\right) \right. \\ \left. - \frac{R_L^0}{R_L^2} U\left(t - \frac{L+R_L}{c_0}\right) - c_0^{-1} \left(\frac{\underline{i}_s \cdot R_L^0 (\underline{i}_s \cdot R_L^0)}{D_L} \right) \delta\left(t - \frac{L+R_L}{c_0}\right) \right\}. \end{aligned} \quad (\text{A.24})$$

The electric field is obtained from the electric-field impulse response by applying the convolution theorem. This finally yields for the electric field

$$\begin{aligned} \underline{E}(\underline{r}, t) = -\frac{1}{4\pi\epsilon_0} \left\{ \frac{R_0^0}{R_0^2} q\left(t - \frac{R_0}{c_0}\right) - \frac{R_L^0}{R_L^2} q\left(t - \frac{L+R_L}{c_0}\right) \right\} \\ - \frac{Z_0}{4\pi} \left\{ \frac{\underline{i}_s \cdot R_0^0 (\underline{i}_s \cdot R_0^0)}{D_0} I\left(t - \frac{R_0}{c_0}\right) - \frac{\underline{i}_s \cdot R_L^0 (\underline{i}_s \cdot R_L^0)}{D_L} I\left(t - \frac{L+R_L}{c_0}\right) \right\}. \end{aligned} \quad (\text{A.25})$$

In Eq.(A.25), $q(t)$ denotes the charge, i.e.,

$$q(t) = \tilde{I}(t) = \int_0^t I(\tau) d\tau. \quad (\text{A.26})$$

The Magnetic Field

The magnetic-field impulse response is readily obtained from Eq.(A.5). Using the vector identity $\underline{\nabla} \times \underline{A}_i = -\underline{i}_z \times \underline{\nabla} A_i$, we write

$$\underline{H}_i(r, t) = \frac{1}{4\pi D} \underline{i}_z \times \left\{ \underline{R}_0^0 \delta\left(t - \frac{R_0}{c_0}\right) - \underline{R}_L^0 \delta\left(t - \frac{L + R_L}{c_0}\right) \right\}. \quad (\text{A.27})$$

Again using the convolution theorem, the magnetic field is finally given by

$$\underline{H}(r, t) = \frac{1}{4\pi} \left\{ \frac{\underline{i}_z \times \underline{R}_0^0}{D_0} I\left(t - \frac{R_0}{c_0}\right) - \frac{\underline{i}_z \times \underline{R}_L^0}{D_L} I\left(t - \frac{L + R_0}{c_0}\right) \right\}. \quad (\text{A.28})$$